

Supplementary Material for “Mott metal-insulator transitions in pressurized layered trichalcogenides”

Heung-Sik Kim,^{1,2} Kristjan Haule,¹ and David Vanderbilt¹

¹*Department of Physics and Astronomy, Rutgers University, Piscataway, NJ 08854, USA*

²*Department of Physics, Kangwon National University, Chuncheon 24341, Korea*

I. COMPUTATIONAL DETAILS

A. Density functional theory calculations

For unit cell optimizations and relaxations of initial internal coordinates, the Vienna *ab-initio* Simulation Package (VASP), which employs the projector-augmented wave (PAW) basis set^{1,2}, was used for density functional theory (DFT) calculations in this work. 340 eV of plane-wave energy cutoff and $8 \times 6 \times 8$ Monkhorst-Pack k -grid sampling were employed. For the treatment of electron correlations within DFT, a revised Perdew-Burke-Ernzerhof exchange-correlation functional for crystalline solid (PBEsol) was employed³, in addition augmented by on-site Coulomb interactions for transition metal d -orbitals within a simplified rotationally-invariant form of DFT+ U_{eff} formalism⁴. 10^{-4} eV/Å of force criterion was employed for structural optimizations. For test purpose, Ceperley-Alder local density approximation⁵ and the original PBE⁶ functionals were also used.

Structural relaxations for all compounds were performed in the presence of the DFT+ U_{eff} (4 eV) on-site Coulomb interaction and a Néel-type antiferromagnetic order⁷, which gives reasonable agreements of lattice parameters and gap sizes with experimentally observed values^{8,9}. It should be mentioned that, without incorporating magnetism and U_{eff} to open the gap, the volume is severely underestimated for both compounds, especially $\sim 20\%$ smaller in MnPS₃. This observation signifies the role of electron correlations in structural properties of these compounds.

B. Dynamical mean-field theory calculations

A fully charge-self-consistent dynamical mean-field method¹⁰, implemented in Rutgers DFT + Embedded DMFT (eDMFT) Functional code (<http://hauleweb.rutgers.edu/tutorials/>) which is combined with WIEN2K code¹¹, is employed for computations of electronic properties and optimizations of internal coordinates¹². In DFT level the Perdew-Wang local density approximation (LDA) is employed, which was argued to yield the best agreement of lattice properties combined with DMFT¹³. 500 k -points were used to sample the first Brillouin zone with $RK_{\text{max}} = 7.0$. A force criterion of 10^{-4} Ry/Bohr was adopted for optimizations of internal coordinates. A continuous-time quantum Monte Carlo method in the hybridization-expansion limit (CT-HYB) was used to solve the auxiliary quantum impurity problem¹⁴, where the full 5 d -orbitals of Ni and Mn were chosen as our correlated subspaces in a single-site

DMFT approximation. For the CT-HYB calculations, up to 10^{10} Monte Carlo steps were employed for each Monte Carlo run. In most runs temperature was set to be 232K, but in some calculations with high pressure it was increased up to 580K because of the increased hybridization between the impurity and bath. -10 to +10 eV of hybridization window (with respect to the Fermi level) was chosen, and $U = 10$ eV and $J_{\text{H}} = 1$ eV of on-site Coulomb interaction parameters were used for both Mn and Ni d -orbitals. A simplified Ising-type (density-density terms only) Coulomb interaction was employed in this work, and it was tested that the use of full Coulomb interaction yields only quantitatively different results in terms of pressure-induced evolution of electronic structures; see Sec. III for more details. A nominal double counting scheme was used, with the d -orbital occupations for double counting corrections for Ni and Mn were chosen to be 8 and 5, respectively.

We comment that the choice of optimal values of the Coulomb interaction U is method-dependent. Other than the eDMFT approach chosen in this study, there are two widely employed first-principles methods using U to incorporate electron correlations; (a) DFT+ U , and (b) DFT+DMFT with Wannierized correlated orbitals. Both methods use smaller values of U ($\simeq 4$ eV) for the correlated d orbitals in transition-metal compounds compared to eDMFT (10 eV)^{15,16}. First, unlike in DFT+ U , in DFT+DMFT formalisms all (local) dynamic screening processes are included via exactly solving the many-body impurity problem. Being such screening processes explicitly treated within DFT+DMFT means that, the input Coulomb interaction U should be closer to the bare one (only screened by the core and semi-core states). In DFT+ U , on the contrary, one should use the screened U (whose value smaller than the DMFT U) to compensate the missing screening processes therein. Hence the U values employed in our eDMFT results are larger than the values used in DFT+ U_{eff} calculations.

Secondly, for DFT+DMFT with Wannierized correlated orbitals, it is well known that the Wannier functions contain a substantial amount of p character from anions (oxygen or chalcogen ions) if a narrow Wannierization energy window that contains only the correlated subspace is chosen. Consequently the critical U becomes much smaller because of the mixing of p character, to be indeed of the order of the bandwidth W . Note that this approach is equivalent to solving Hubbard-type models, where only correlated orbital degrees of freedom are considered.

Contrary to the aforementioned approaches, in the eDMFT formalism we are solving a generalized Anderson-lattice type Hamiltonian (actually the p - d type Hamiltonian), where the effective U_{eff} that could be compared with the Hubbard- U in

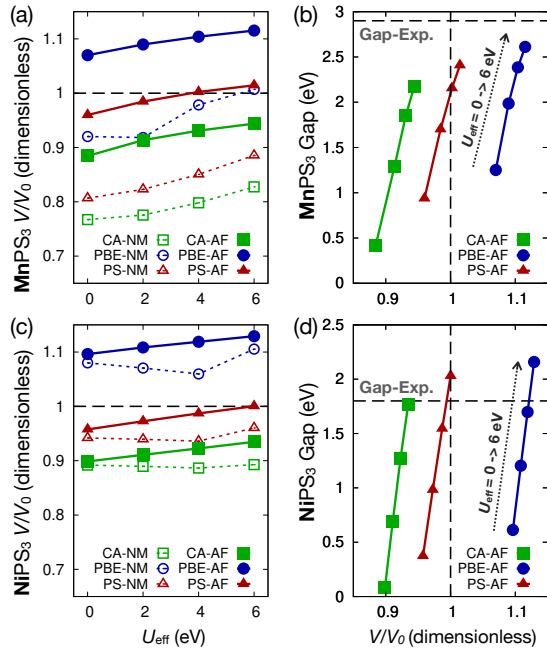


FIG. S1. Calculated unit cell volumes and band gap sizes of (a,b) MnPS_3 and (c,d) NiPS_3 under different choices of exchange-correlation (XC) functionals, the presence of antiferromagnetic order, and U_{eff} values at the ambient pressure condition (*i.e.* optimizing cell volume without any volume/shape constraint). (a,c) show how the cell volume depends on the choice of XC functionals, the presence of antiferromagnetic order, and U_{eff} values for each compound, and (b,d) show the size of gap as a function of cell volume with respect to the choice of XC functionals. Therein 4 data points for each XC functional, from bottom to top, represent results with $U_{\text{eff}} = 0, 2, 4,$ and 6 eV respectively. In the legend PS, NM, AF denote PBEsol, nonmagnetic, and antiferromagnetic orders respectively. Néel- and zigzag-type AF order were employed for MnPS_3 and NiPS_3 , respectively. V_0 denotes experimental cell volume for each compound⁷, and horizontal black dashed lines in (b,d) show experimentally measured gap sizes.

the Hubbard-type model is actually the p - d splitting. The advantage of using such p - d type Hamiltonian in DFT+DMFT is evident; the U values in such models are much more system-independent for many transition-metal compounds, as demonstrated recently^{15,16}. Therein we established that a reasonable U for a wide range of transition-metal oxides within the eDMFT (*i.e.* the p - d model with very localized d orbitals described above) is around 10 eV and $J = 1$ eV, and is much more universal than the U values in downfolded Hubbard-like models.

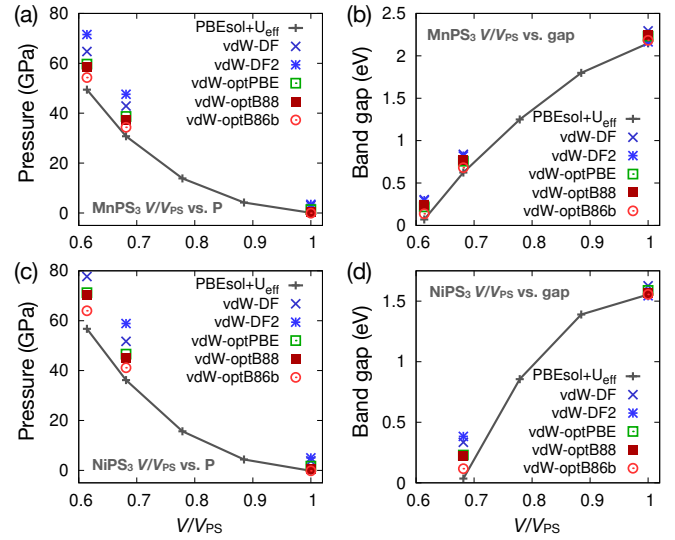


FIG. S2. Dependence of crystal and electronic structures on five van der Waals (vdW) functionals (see the text) for (a,b) MnPS_3 and (c,d) NiPS_3 . Colored symbols represent vdW functional results, and PBEsol+ U_{eff} (4 eV) results (dark gray curves) are shown as a reference. In panel (a) and (c), the calculated pressure P is shown as a function of dimensionless volume (V/V_{Ps} , where V_{Ps} is the computed ambient-condition volume with PBEsol+ $U_{\text{eff}} = 4$ eV). In panel (b) and (d), band gap is shown as a function of V/V_{Ps} .

II. EXCHANGE-CORRELATION AND VAN DER WAALS FUNCTIONAL DEPENDENCE WITHIN DFT+ U_{eff}

A. Dependence on exchange-correlation functionals and U_{eff} -value in DFT+ U_{eff} results

Fig. S1 shows how MnPS_3 and NiPS_3 behave under the choice of different exchange-correlation functionals and the value of U_{eff} , where experimental cell volumes and gap sizes are from Ref. 7, 9, and 17. Fig. S1(a) and (c) show how the cell volume depends on the choice of exchange-correlation (XC) functionals, the presence of antiferromagnetic (AF) order, and the U_{eff} values for each compound. We notice that *i*) the absence of AF order, which prevents the formation of high-spin configurations in both compounds, yields significantly underestimated cell volumes in all cases. Such behavior is more evident in MnPS_3 , where the absence of magnetism leads to the low-spin configuration that favors intermetallic bonding. *ii*) the PBEsol XC functional gives better agreement with experimental volume than CA or PBE, and using $U_{\text{eff}} = 4 \sim 6$ eV in the PBEsol+ U_{eff} setup produces the best fit. The same conclusion can be also made from the gap-volume dependence shown in Fig. S1(b) and (d), where the use of PBEsol+ U_{eff} (4 eV) yields the best fit of gap size and cell volume for both compounds. Overall, employing PBEsol+ U_{eff} (4 eV) does seem reasonable for studying pressurized MnPS_3 and NiPS_3 .

B. van der Waals functional dependence

Fig. S2 presents how the estimated pressure and the size of Kohn-Sham energy gap at a given volume depend on the choice of van der Waals (vdW) functionals in MnPS_3 and NiPS_3 . The range of unit cell volume is chosen to be $0.6V_{\text{PS}} \leq V \leq 1.0V_{\text{PS}}$, where V_{PS} is the ambient-pressure cell volume optimized with $\text{PBEsol}+U_{\text{eff}}$ (4 eV). We employed 5 different vdW functionals implemented in VASP; vdW-DF¹⁸, vdW-DF2¹⁹, optPBE, optB88, and optB86b²⁰. For both compounds, different functionals tend to give similar results, while NiPS_3 shows more noticeable functional dependence compared to MnPS_3 . It can be speculated that, in NiPS_3 with an open-shell Ni e_g orbitals, the unquenched orbital degree of freedom makes the system a bit more sensitive to the treatment of correlations. Nevertheless the qualitative features we address in this manuscript, the pressure-driven insulator-to-metal transitions and their orbital dependence, remain basically the same as shown in Fig. S2(b) and (d).

Specifically we notice that vdW functionals, except vdW-DF and vdW-DF2 functionals, show reasonable agreements with PBEsol results. vdW-DF and vdW-DF2 functionals tends to prefer larger volume (*i.e.* larger P estimated at the same volume compared to other functionals). This is because these functionals favor larger interlayer distances in the high-pressure regime than conventional XC functionals. Overall, even though use of different vdW functional induces some quantitative differences, it does not seem to change our main conclusions in this work.

We comment that, since vdW functionals favor larger cell volume, the inclusion of them should enhance the magnitude of critical pressures for structural/electronic transitions in both compounds, which is actually making the discrepancy between the theoretical prediction and experimental observation slightly worse in MnPS_3 . Hence we argue that $\text{PBEsol}+U_{\text{eff}}$ can be a more reasonable choice in this pressurized setup where the direct orbital overlap between layers becomes significant.

III. COMPARISON WITH $\text{DFT}+U_{\text{eff}}$ AND DMFT

Table I presents the comparison between $\text{PBEsol}+U_{\text{eff}}$ - and eDMFT-optimized atomic coordinates of MnPS_3 and NiPS_3 , both at ambient and high-pressure regimes. Here ambient and high-pressure results represent Mott-insulating and weakly correlated metallic phases, respectively, for both compounds. In eDMFT calculations, as commented in the manuscript, optimized cell parameters **a**, **b**, **c**, and monoclinic angle β from $\text{PBEsol}+U_{\text{eff}}$ were employed. This is due to the absence of stress tensor formalism implemented in any of full-potential linearized augmented plane wave codes, and in $\text{DFT}+\text{DMFT}$ formalisms as well. Under this constraint, eDMFT-optimized atomic coordinates show very similar results with $\text{PBEsol}+U_{\text{eff}}$ ones despite different magnetization conditions; paramagnetic order for eDMFT, and antiferromagnetism (Néel order for MnPS_3 , zigzag order for NiPS_3) in $\text{PBEsol}+U_{\text{eff}}$.

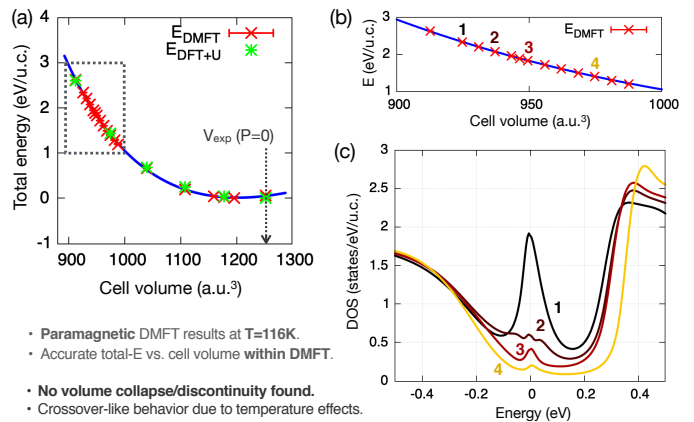


FIG. S3. (a) Calculated energy versus volume plot for NiPS_3 . Bright green and red symbols represent data points from $\text{PBEsol}+U_{\text{eff}}$ and eDMFT results respectively. Sizes of error bars in eDMFT points ($\lesssim 5$ meV) are smaller than the symbol size. Blue curve is from the Birch-Murnaghan fit of eDMFT energies. Note that eDMFT result predicts slightly smaller ambient-pressure volume compared to experimental value. (b) A magnification of the eDMFT energy-volume data close to the insulator-to-metal transition, where the area of magnification indicated as a gray dashed box in (a). (c) Real-frequency spectral weights at different volumes close to the insulator-to-metal transition. Colored number for each curve indicates at which volume the spectral function was taken (see (b)). Calculated pressures at point 1 and 2 from the Birch-Murnaghan fit are 24.3 and 22.2 GPa, respectively.

However, the validity of employing $\text{DFT}+U_{\text{eff}}$ with a magnetic order in optimizing crystal structures of paramagnetic systems, especially the cell parameters, may need to be checked. This is because, like in MnPS_3 as shown in the manuscript, some structural phase transitions are strongly coupled to elastic deformations of the unit cell. One may even suspect that the discrepancy between the predicted and experimentally reported⁸ critical pressures of the structural transition in MnPS_3 might originate from the use of magnetic $\text{DFT}+U_{\text{eff}}$ in optimizing the unit cell size and shape.

To resolve the issue mentioned above, energy landscapes from $\text{DFT}+U_{\text{eff}}$ and eDMFT in the cell parameter space need to be compared with each other. Even though full structural relaxations may not be possible within eDMFT formalism, several trials to compare $\text{DFT}+U_{\text{eff}}$ - and DMFT-optimized structures were performed, where DMFT calculations were done in the paramagnetic configuration.

A. NiPS_3

According to our result presented in the manuscript, NiPS_3 does not have a noticeable structural change at the MIT pressure of $P \simeq 30$ GPa, which is somewhat unusual. Hence, for a closer look on the structure-free MIT point, we computed a total energy curve versus cell volume for paramagnetic (PM) eDMFT near the MIT. For more accurate results, the rotationally invariant form of the Coulomb interaction (spin-flip and

		MnPS ₃				NiPS ₃					
V/V_{PS}		1.00	0.56			1.00	0.56				
P_{DFT} (GPa)		0.0	49.8			0.0	88.0				
a		6.025	4.916			5.761	5.173				
b		10.436	8.845			9.977	8.531				
c (Å)		6.870	5.542			6.736	4.938				
β (degree)		106.67	108.72			106.64	110.17				
		DFT+ U_{eff}	eDMFT	DFT+ U_{eff}	eDMFT	DFT+ U_{eff}	eDMFT	DFT+ U_{eff}	eDMFT		
Mn (4 <i>g</i>)	<i>y</i>	0.3327	0.3326	0.3589	0.3585	Ni (4 <i>g</i>)	<i>y</i>	0.3333	0.3329	0.3339	0.3344
P (4 <i>i</i>)	<i>x</i>	0.0550	0.0552	-0.0376	-0.0256	P (4 <i>i</i>)	<i>x</i>	0.0570	0.0573	0.0803	0.0790
	<i>z</i>	0.1674	0.1683	0.1719	0.1770		<i>z</i>	0.1677	0.1687	0.2223	0.2199
S1 (4 <i>i</i>)	<i>x</i>	0.7551	0.7431	0.6707	0.6831	S1 (4 <i>i</i>)	<i>x</i>	0.7346	0.7378	0.7299	0.7324
	<i>z</i>	0.2474	0.2512	0.3409	0.3539		<i>z</i>	0.2371	0.2420	0.2948	0.2995
S2 (8 <i>j</i>)	<i>x</i>	0.2441	0.2448	0.2426	0.2463	S2 (8 <i>j</i>)	<i>x</i>	0.2523	0.2467	0.2990	0.2988
	<i>y</i>	0.1628	0.1625	0.1858	0.1855		<i>y</i>	0.1727	0.1719	0.1930	0.1923
	<i>z</i>	0.2485	0.2525	0.2617	0.2781		<i>z</i>	0.2366	0.2422	0.2909	0.2955

TABLE I. Optimized lattice parameters of MnPS₃ and NiPS₃ from DFT+ U_{eff} and eDMFT results, both at ambient and high-pressure regimes. Ambient and high-pressure results represent Mott-insulating and weakly correlated metallic phases, respectively, for both compounds. PBEsol+ $U_{\text{eff}} = 4$ eV was adopted for DFT+ U_{eff} . Cell parameters (**a**, **b**, **c**, and β) optimized in DFT+ U_{eff} calculations were employed in eDMFT ones. Nonzero components of Wyckoff positions of the $C2/m$ space group are shown. All eDMFT calculations were done at $T = 232$ K except the high-pressure ($V = 0.56V_{\text{PS}}$) MnPS₃ one, where $T = 580$ K was used for computational issues. V_{PS} denotes the ambient pressure cell volume for both compounds, obtained with PBEsol+ $U_{\text{eff}} = 4$ eV

pair-hopping included) was employed at a lower temperature of $T = 116$ K. PM MIT is usually known to accompany a sudden volume change (as reported in Ref. 35 in the manuscript, for example), which should be captured as a discontinuity in the energy-volume curve at the MIT point. Figure S3 shows a summary of the results; note that all the data points were obtained from calculations started from scratch to capture both the metallic and insulating phases (with optimized internal parameters). It can be seen that both the PBEsol+ U_{eff} and DFT+DMFT data points remarkably collapse onto a single Birch-Murnaghan energy-volume curve (Fig. S3(a)), and that no discontinuity can be noticed near the MIT point (Fig. S3(b) and (c)). Note that the use of the additional Coulomb interaction with the spin-flip and pair-hopping terms (hereafter denoted as ‘beyond-Ising’ terms) lowered the MIT critical pressure from 31 to 24 GPa. The crossover-like behavior can be attributed to the temperature effect, but due to the computational cost issue the temperature could not be lowered below $T = 116$ K.

B. MnPS₃

As marked in Fig. 1(a) in the main text, the value of critical pressure predicted by PBEsol+ U_{eff} calculations is twice bigger than the one reported in Ref. 8 (63 vs. 30 GPa). For a better understanding of this discrepancy, we perform calculations with interpolating structures between the honeycomb high-spin and the dimerized low-spin structures as shown in Fig. S4. Because the computation of stress tensor is not

yet available in the current eDMFT formalism, two constant-volume cuts at $V = 0.57$ and $0.54 V_0$ are taken for a total energy comparison as shown in Fig. S4(a). For PBEsol+ U_{eff} results, high-spin and low-spin states are first converged in their honeycomb and dimerized structures respectively, and then the crystal structures are slowly distorted towards the other side while maintaining the local minima spin states.

Fig. S4(b) and (c) are relative total energies and size of spin moments from the high-, low-spin PBEsol+ U_{eff} , and paramagnetic eDMFT calculations at $V = 0.57 V_0$. A remarkable feature is, while the energy difference between the high- and low-spin ground states is 1.72 eV in PBEsol+ U_{eff} , it is 0.58 eV in eDMFT, which is almost one third of the PBEsol+ U_{eff} value. Furthermore, while the high- and low-spin local minima states remain (meta)stable even after the structural changes, as shown in Fig. S4(c), in eDMFT we have a spin-state crossover as the structure evolve from one limit to another. This features persist at $V = 0.54 V_0$ (Fig. S4(d,e)), where the height of the energy barrier from the high-spin to the low-spin state (0.3 eV) is substantially suppressed (60 meV) with the same spin-state crossover. These observations show that, the dynamical fluctuation effect inherent in eDMFT causes mixing between different spin configurations, hence introducing the crossover behavior shown in Fig. S4(c) and (e) and suppressing the energy differences. This observation is consistent with a previous DFT+DMFT study on a spin-state-crossover molecule²¹. Note that, our analysis here does not explicitly predict that the low-spin state is stabilized at lower pressure in eDMFT results shown in Fig. 1(a) in the main text. However, since the energy difference between different states

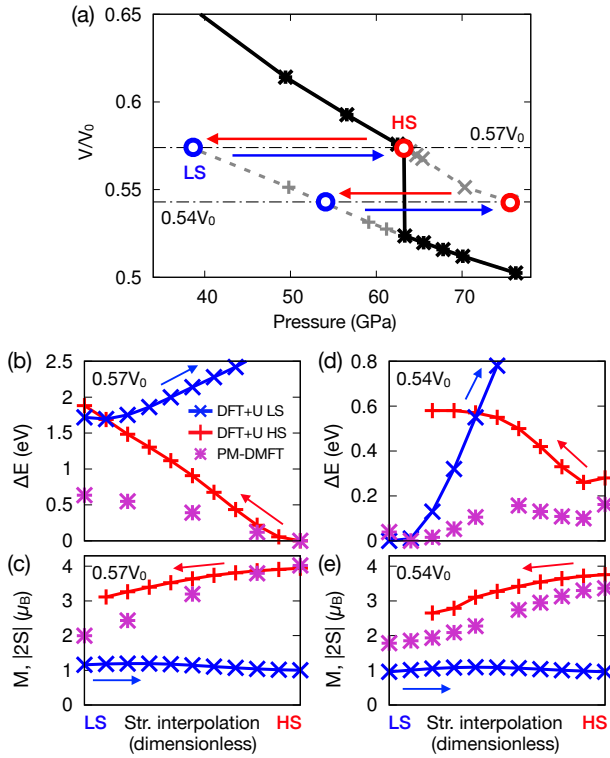


FIG. S4. (a) A magnified view of the MnPS₃ volume vs. pressure plot, where the black solid and gray dashed lines are curves for ground and metastable states respectively. Two dash-dotted lines are at $V = 0.57 V_0$ and $0.54 V_0$ on which structural interpolations between the high-spin honeycomb and low-spin dimerized structures are made. (b,c) Total energy differences (b) and size of Mn moments (c) as a function of structural interpolation at $V = 0.57 V_0$, where red (blue) curve depicting total energy and Mn magnetization starting from high-spin (low-spin) structure and approaching to the low-spin (high-spin) side, and purple symbols depicting same results from paramagnetic eDMFT calculations at $T = 580$ K. (d,e) Same plots at $V = 0.54 V_0$. Size of QMC error bars for eDMFT results are 4 meV at most, smaller than the symbol size.

is reduced to a fraction compared to PBEsol+ U_{eff} results, the value of critical pressure might be reduced after the lattice free energy contribution and the zero-point fluctuation ignored in this work are included.

We comment that, due to the increased computational cost of the CT-HYB impurity solver by the enhanced intermetallic hybridization in the pressurized setup, all eDMFT data points presented in Fig. S4 were obtained at $T = 580$ K. Even without the beyond-Ising Coulomb terms, which significantly increases sign problems in the impurity solver stage, the temperature could not be lowered due to the computational cost issue. Therefore we could not check all the results with employing the beyond-Ising Coulomb terms. As a partial check, we have done two eDMFT calculations for MnPS₃, employing two lattice parameter sets (a, b, c, and the monoclinic angle β) corresponding to non-dimerized metallic and dimerized Mott-insulating states around 50 GPa. Initial internal coordinates, optimized within eDMFT afterwards, were adopted from the ambient pressure structure. The purpose of this comparison

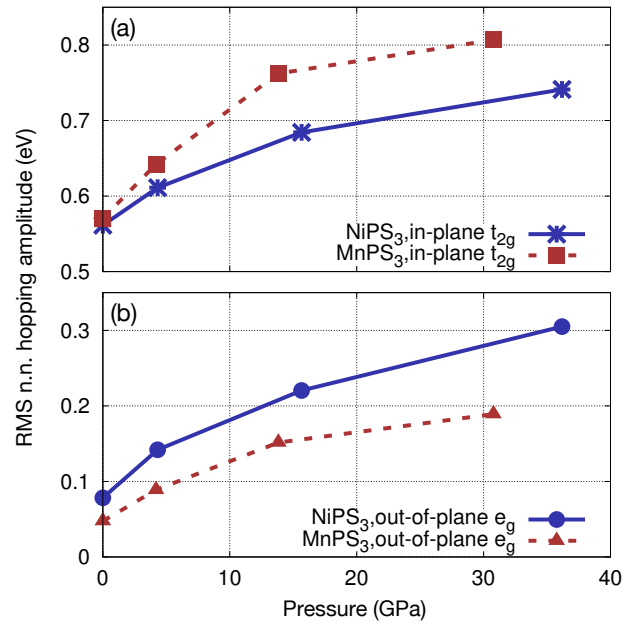


FIG. S5. Root mean square (RMS) of nearest-neighbor (n.n.) Wannier hopping amplitudes for Ni and Mn d -orbitals as a function of pressure, where the RMS of (a) in-plane t_{2g} - t_{2g} and (b) out-of-plane e_g - e_g are shown.

is to see whether the choice of different Coulomb interactions yields noticeable difference. Table II summarizes the optimized structures with Ising and beyond-Ising Coulomb interactions, which shows negligible difference with respect to each other. Hence we are safe to use Ising form in this case.

IV. IN-PLANE AND OUT-OF-PLANE HOPPING AMPLITUDES

Fig. S5(a) and (b) show root mean square (RMS) amplitudes of nearest-neighbor (n.n.) in-plane t_{2g} and out-of-plane e_g hopping integrals, respectively, for MnPS₃ and NiPS₃. The d -orbital hopping integrals were computed using WANNIER90 package²², employing optimized crystal structures in the presence of external pressure, without including U_{eff} and magnetism.

As shown in Fig. 1(a) and (b) in the main text, the in-plane lattice parameters (with respect to their ambient pressure value) a/a_0 and b/b_0 for MnPS₃ around 30 GPa are smaller by $\sim 2\%$ compared to those of NiPS₃, while the out-of-plane c/c_0 of MnPS₃ is larger than that of NiPS₃. In accordance with the tendency of lattice parameter changes, the enhancement of RMS in-plane t_{2g} hopping integrals is more pronounced in MnPS₃, which drives the formation of in-plane Mn dimer formation after the transition to the low-spin state with the open t_{2g} shell. Note that, the in-plane t_{2g} hopping integrals for Ni is also enhanced as the pressure is increased, but its effect is not significant due to the closed t_{2g} shell in the Ni d^8 configuration. Similarly, the enhanced out-of-plane kinetic energy between the e_g orbitals in NiPS₃, depicted in

	Dimerized			Non-dimer		
V	0.55 V_{PS}			0.61 V_{PS}		
P_{PS}	49.8 GPa			49.4 GPa		
\mathbf{a}/\mathbf{a}_0	0.8159			0.8619		
\mathbf{b}/\mathbf{b}_0	0.8475			0.8653		
\mathbf{c}/\mathbf{c}_0	0.8066			0.8263		
β	108.72°			107.32°		
Coulomb	Ising	Beyond-Ising		Ising	Beyond-Ising	
Mn (4g)	(0.0000, 0.1415, 0.0000)	(0.0000, 0.1407, 0.0000)		(0.0000, 0.1664, 0.0000)	(0.0000, 0.1661, 0.0000)	
P (4i)	(0.5256, 0.0000, 0.8230)	(0.5278, 0.0000, 0.8238)		(0.4358, 0.0000, 0.8064)	(0.4358, 0.0000, 0.8063)	
S1 (4i)	(0.8170, 0.0000, 0.6461)	(0.8176, 0.0000, 0.6451)		(0.2598, 0.0000, 0.6964)	(0.2603, 0.0000, 0.6961)	
S2 (8j)	(0.7538, 0.3145, 0.7219)	(0.2542, 0.3142, 0.7227)		(0.2231, 0.3205, 0.6980)	(0.2228, 0.3201, 0.6984)	

TABLE II. Optimized crystal structures of MnPS_3 under different volume constraints ($V = 0.55V_{\text{PS}}$ and $0.61V_{\text{PS}}$, where V_{PS} and P_{PS} are optimized ambient-pressure volume and exerted pressure at a fixed volume from PBEsol+ U_{eff} (4 eV) results. Equilibrium lattice parameters from PBEsol+ U_{eff} calculations are given as $(\mathbf{a}_0, \mathbf{b}_0, \mathbf{c}_0, \beta_0) = (6.025\text{\AA}, 10.436\text{\AA}, 6.870\text{\AA}, 106.67^\circ)$. Internal coordinates optimized from eDMFT calculations, with different choices of Coulomb interactions (Ising vs. beyond-Ising), are listed below.

Fig. S5(b), induces more pronounced reduction of the c parameter in NiPS_3 compared to that of MnPS_3 . It should be mentioned that, while the out-of-plane e_g hopping terms are also enhanced in MnPS_3 , their role in structural response to pressure is less significant both in the low- and high-pressure regimes; in the low-pressure regime the hybridization between the d^5 high-spin Mn ion and anions is weak, and so is the electron-lattice coupling, while in the high-pressure regime the high-spin Mn has empty e_g shell.

V. ELECTRONIC STRUCTURES WITH A NÉEL ORDER

A. Ambient pressure cases for both compounds

Fig. S6 shows the spectral functions of NiPS_3 (a-c) and MnPS_3 (d-f) with a Néel-type antiferromagnetic (AF) order in comparison with the paramagnetic (PM) phases. In both compounds, the presence of magnetism does not alter the size of charge gap, consistent with the Mott character of the insulating phases in both compounds. As the temperature is lowered and magnetism sets in, the broadening of spectral functions due to the imaginary part of self-energy is weakened. Indeed, DFT+ U_{eff} PDOS with the magnetic order shows very similar qualitative features with DMFT PDOS at $T=58\text{K}$ (not shown).

Note that, the use of the Ising-type Coulomb repulsion gives rise to the stabilization of magnetic order well above the Néel temperatures of both compounds, $T_N = 154$ and 78 K for NiPS_3 and MnPS_3 , respectively^{7,23,24}, as reported in previous DFT+DMFT studies²⁵. It is argued that a larger in-plane kinetic energy scale originating from the e_g orbital in Ni yields the higher T_N in NiPS_3 compared to MnPS_3 ⁹. Despite the overestimated T_N , such tendency can be noticed in our results by comparing Fig. S6(b) and (e). While the size of the Ni magnetization in NiPS_3 ($2S_{\text{Ni}} = 1.45 \mu_B$) is almost saturated to the value of PM moment ($|2S_{\text{Ni}}| = 1.65 \mu_B$), even at $T = 232\text{K}$, the Mn magnetization in MnPS_3 at the same T is

$2S_{\text{Mn}} = 0.87 \mu_B$, just a fraction of the $S = 5/2$ moment size ($4.80 \mu_B$) of the high-spin Mn. As T is lowered to 58K , magnetizations in both compounds saturate to the local moment size, as shown in Fig. S6(c) and (f).

B. Near the MIT critical pressure

1. MnPS_3

As discussed in the main text, the pressure-induced MIT in MnPS_3 in the paramagnetic phase is a discontinuous transition accompanied by a spin-state transition and isosymmetric structural distortion with a volume collapse. Such discontinuous character does not change in the presence of magnetism, as shown in Fig. S8, where the change of the Mn magnetization M (per Mn) from DFT+ U_{eff} and eDMFT results (at $T = 232$ K) are shown as a function of pressure. Note that, the upturn of M in the small-pressure regime (< 10 GPa) in eDMFT is due to the enhancement of magnetic exchange interactions originating from increased kinetic energy scale under the pressure.

2. NiPS_3

In the PM phase of NiPS_3 , the MIT can be indicated not only by the gap opening in the PDOS, but also by the change of electron self-energies $\Sigma(\omega)$. In Fig. S7(a) and (c), the MIT can be noticed by the presence and absence of the dip at the Fermi level in their PDOS, but it is slightly unclear whether the phase at $P = 30.4$ GPa is an insulator due to the small but finite e_g DOS at the Fermi level due to the broadening. However, $\Im\Sigma(\omega)$, plotted in Fig. S7(b) and (d), show a clear difference between the two phases, because the presence (absence) of a pole at the Fermi level in the e_g - $\Im\Sigma(\omega)$ signifies the presence (absence) of the Mott physics.

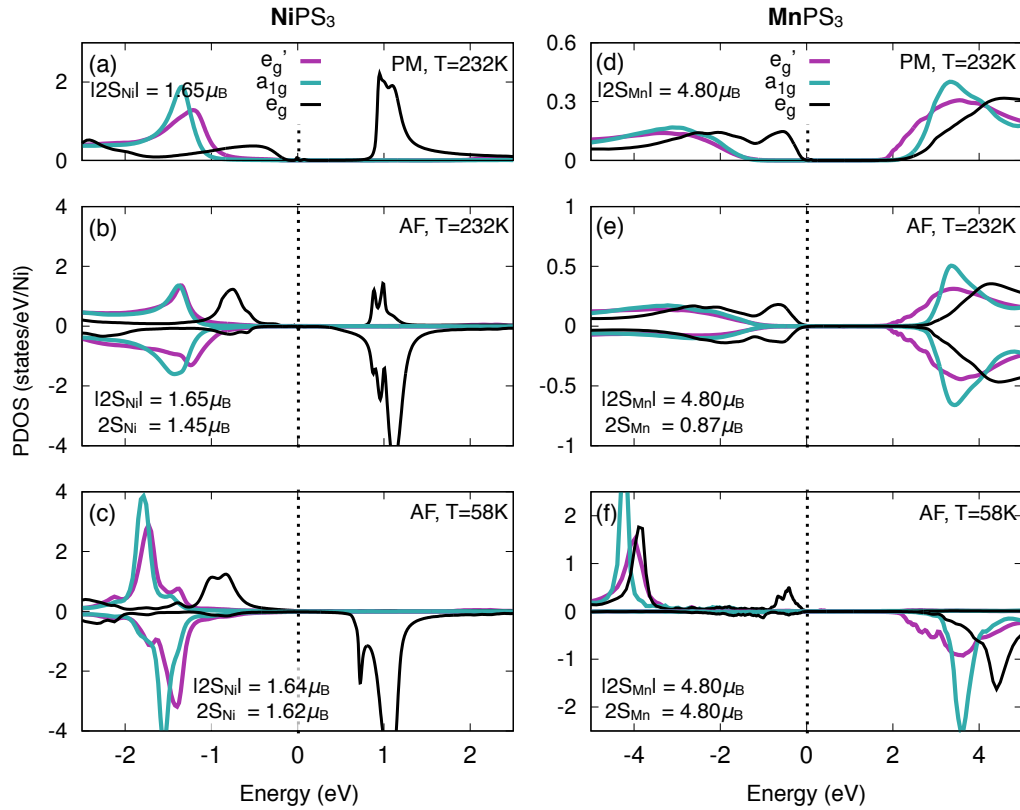


FIG. S6. (a-c) PDOS of NiPS₃ and (d-f) MnPS₃ with a Néel type antiferromagnetic (AF) order (b,c,e,f) in comparison with paramagnetic (PM) PDOS (a,d). The second and third rows show AF PDOS with $T = 232\text{K}$ and 58K , respectively.

In the AF-ordered phases, the gap opening is induced by the exchange splitting between the spin up and down components, *i.e.* $\Re(\Sigma_{\text{up}} - \Sigma_{\text{down}})(\omega)$. In cases where $\Im\Sigma(\omega)$ is weak compared to $\Re\Sigma(\omega)$ and the frequency dependence of $\Re(\Sigma_{\text{up}} - \Sigma_{\text{down}})(\omega)$ is small, then the eDMFT results become equivalent to the DFT+ U_{eff} results. Fig. S7(e-j) present such situation, where the PDOSs shown in Fig. S7(e) and (h) become qualitatively equivalent to DFT+ U_{eff} PDOS (not shown), with the exchange splitting of $\sim 4\text{ eV}$ at the Fermi level opening a gap for the e_g bands. Hence, in AF phases the MIT critical pressure is mainly determined by the e_g bandwidth and the exchange splitting $\Re(\Sigma_{\text{up}} - \Sigma_{\text{down}})(\omega)$. Because the above quantities change continuously as the pressure is increased, it is not easy to point out at which pressure the MIT happens from the PDOS plots due to the presence of small broadening from $\Im\Sigma(\omega)$. At $T = 232\text{K}$, the MIT seems to happen around 24 GPa, and this pressure does not change as T is lowered to 116K.

Fig. S9(a) depicts the change of Ni magnetizations from

DFT+ U_{eff} and AF-eDMFT as a function of pressure. Note that, the MIT critical pressures are 36 and $24 \sim 30\text{ GPa}$ for DFT+ U_{eff} and AF-eDMFT results, as shown in the figure, but the magnetization persists within the metallic phase. The pressure where the magnetism disappears in AF-eDMFT results increases slightly from 36 to 40 GPa as the T is reduced from 232K to 116K, but it does not reach 58 GPa where the magnetization disappears in DFT+ U_{eff} results. Note that, the high-pressure anisotropic structural distortion in NiPS₃ happens at the pressure where the DFT+ U_{eff} magnetization becomes zero.

Fig. S9(b) shows the change of Ni local spin moment size $|2S|$ as a function of pressure. Unlike the $|2S|$ in the PM phase, which shows a cusp at the MIT critical pressure, $|2S|$ in the AF phases does not show such behavior at the MIT pressure. As the pressure is increased, the AF $|2S|$ is suppressed until the magnetization disappears and a PM metallic phase happens. Note that, the pressures that AF $|2S|$ joins the PM $|2S|$ curve are the points where the magnetization disappears.

¹ G. Kresse and J. Hafner, “*Ab initio* molecular dynamics for liquid metals,” *Phys. Rev. B* **47**, 558–561 (1993).

² G. Kresse and J. Furthmüller, “Efficient iterative schemes for *ab initio* total-energy calculations using a plane-wave basis set,” *Phys. Rev. B* **54**, 11169–11186 (1996).

³ John P. Perdew, Adrienn Ruzsinszky, Gábor I. Csonka, Oleg A. Vydrov, Gustavo E. Scuseria, Lucian A. Constantin, Xiaolan Zhou, and Kieron Burke, “Restoring the density-gradient expansion for exchange in solids and surfaces,” *Phys. Rev. Lett.* **100**, 136406 (2008).

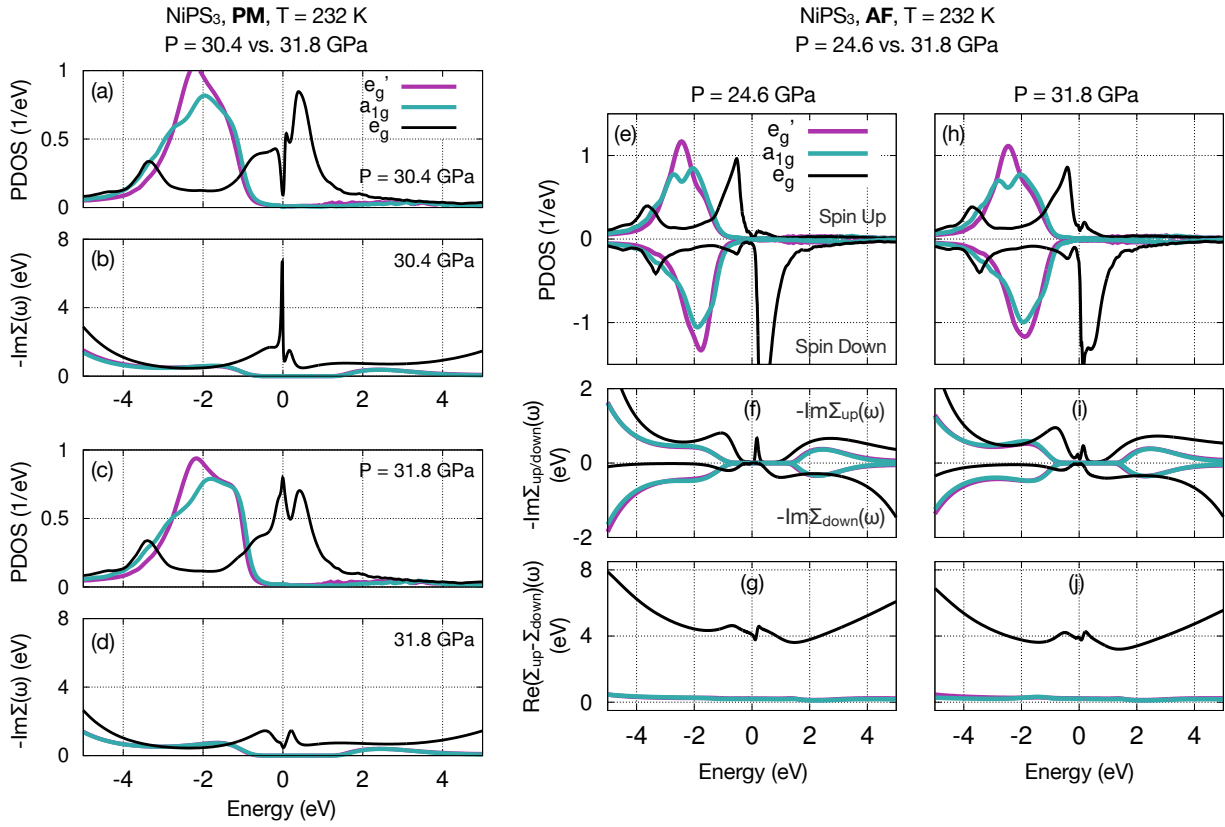


FIG. S7. PDOS and electron self-energies $\Sigma(\omega)$ of (a-d) PM and (e-j) AF NiPS₃ at $T = 232$ K. The imaginary part of PM self-energies in (b) and (d) show a clear e_g peak and its absence in the Mott-insulating and metallic phases, respectively. (e) and (h) show spin- and orbital-projected PDOS at $P = 24.6$ and 31.8 GPa, respectively (spin up and down PDOS plotted in positive and negative values respectively). Imaginary part of $\Sigma(\omega)$, plotted in (f) and (i), show the absence of peak near the Fermi level. (e) and (h) show the difference between the real part of spin up and down self-energies $\Re(\Sigma_{\text{up}} - \Sigma_{\text{down}})(\omega)$, which is the on-site exchange splitting opening the gap in the magnetic phases. Note that, the MIT point is not clear due to the smearing of spin up and down e_g bands in the PDOS.

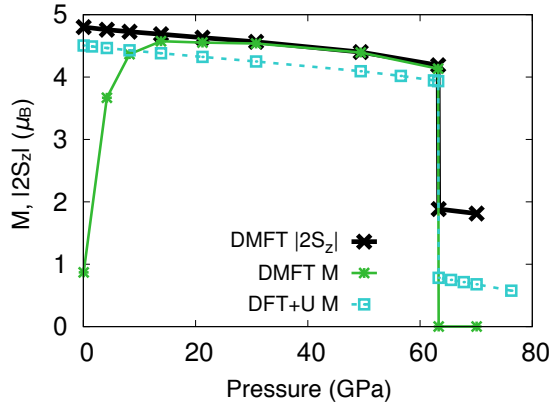


FIG. S8. Evolution of sizes of DFT+ U_{eff} and eDMFT local moments $|2S_z|$ and Mn magnetization M (per Mn) in MnPS₃ as a function of pressure. eDMFT results are obtained at $T = 232$ K with the Néel order.

⁴ S. L. Dudarev, G. A. Botton, S. Y. Savrasov, C. J. Humphreys, and A. P. Sutton, “Electron-energy-loss spectra and the structural stability of nickel oxide: An LSDA+ U study,” *Phys. Rev. B* **57**,

1505–1509 (1998).

⁵ D. M. Ceperley and B. J. Alder, “Ground state of the electron gas by a stochastic method,” *Phys. Rev. Lett.* **45**, 566–569 (1980).

⁶ John P. Perdew, Kieron Burke, and Matthias Ernzerhof, “Generalized gradient approximation made simple,” *Phys. Rev. Lett.* **77**, 3865–3868 (1996).

⁷ Raymond Brec, “Review on structural and chemical properties of transition metal phosphorous trisulfides MPS_3 ,” *Solid State Ion.* **22**, 3–30 (1986).

⁸ Yonggang Wang, Zhengyang Zhou, Ting Wen, Yannan Zhou, Nana Li, Fei Han, Yuming Xiao, Paul Chow, Junliang Sun, Michael Pravica, Andrew L. Cornelius, Wenge Yang, and Yusheng Zhao, “Pressure-driven cooperative spin-crossover, large-volume collapse, and semiconductor-to-metal transition in manganese(ii) honeycomb lattices,” *J. Am. Chem. Soc.* **138**, 15751–15757 (2016).

⁹ So Yeun Kim, Tae Yun Kim, Luke J. Sandilands, Soobin Sinn, Min-Cheol Lee, Jaeseok Son, Sungmin Lee, Ki-Young Choi, Wondong Kim, Byeong-Gyu Park, C. Jeon, Hyeong-Do Kim, Cheol-Hwan Park, Je-Geun Park, S. J. Moon, and T. W. Noh, “Charge-spin correlation in van der waals antiferromagnet NiPS₃,” *Phys. Rev. Lett.* **120**, 136402 (2018).

¹⁰ Kristjan Haule, Chuck-Hou Yee, and Kyoo Kim, “Dynamical mean-field theory within the full-potential methods: Electronic structure of CeIrIn₅, CeCoIn₅, and CeRhIn₅,” *Phys. Rev. B* **81**,

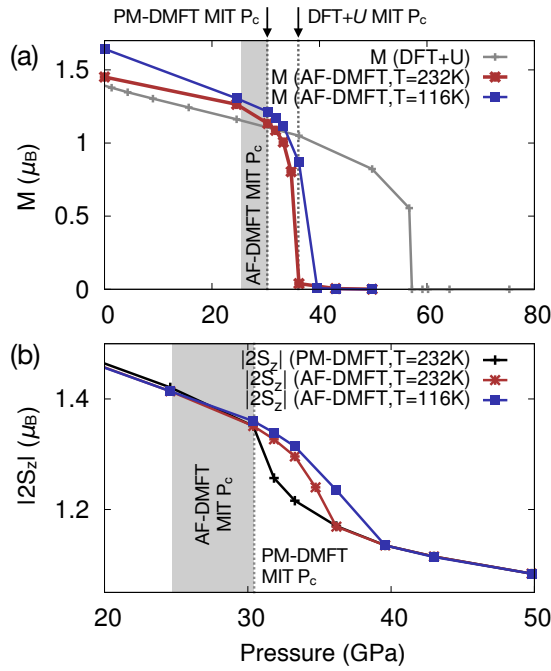


FIG. S9. (a) Evolution of Ni magnetization M (per Ni) from $DFT+U_{\text{eff}}$ (gray curve), AF-eDMFT at $T = 232$ (red) and $58K$ (blue) as a function of pressure. The MIT critical pressures from $DFT+U_{\text{eff}}$, PM- and AF-eDMFT are depicted. (b) Sizes of Ni spin moments $|2S_z|$ from PM- and AF-eDMFT results.

195107 (2010).

- ¹¹ P. Blaha, K. Schwarz, G. K. H. Madsen, D. Kvasnicka, and J. Luitz, *WIEN2k, An Augmented Plane Wave + Local Orbitals Program for Calculating Crystal Properties* (Karlheinz Schwarz, Techn. Universität Wien, Austria, 2001).
- ¹² Kristjan Haule and Gheorghe L. Pascut, “Forces for structural optimizations in correlated materials within a DFT+embedded DMFT functional approach,” *Phys. Rev. B* **94**, 195146 (2016).
- ¹³ Kristjan Haule and Turan Birol, “Free energy from stationary implementation of the DFT + DMFT functional,” *Phys. Rev. Lett.* **115**, 256402 (2015).

- ¹⁴ Kristjan Haule, “Quantum monte carlo impurity solver for cluster dynamical mean-field theory and electronic structure calculations with adjustable cluster base,” *Phys. Rev. B* **75**, 155113 (2007).
- ¹⁵ Kristjan Haule, Turan Birol, and Gabriel Kotliar, “Covalency in transition-metal oxides within all-electron dynamical mean-field theory,” *Phys. Rev. B* **90**, 075136 (2014).
- ¹⁶ Subhasish Mandal, Kristjan Haule, Karin M. Rabe, and David Vanderbilt, “Systematic beyond-dft study of binary transition metal oxides,” *arXiv preprint arXiv:1907.10498* (2019).
- ¹⁷ V. Grasso, F. Neri, P. Perillo, L. Silipigni, and M. Piacentini, “Optical-absorption spectra of crystal-field transitions in mnp_3 at low temperatures,” *Phys. Rev. B* **44**, 11060–11066 (1991).
- ¹⁸ M. Dion, H. Rydberg, E. Schröder, D. C. Langreth, and B. I. Lundqvist, “Van der waals density functional for general geometries,” *Phys. Rev. Lett.* **92**, 246401 (2004).
- ¹⁹ Kyuho Lee, Éamonn D. Murray, Lingzhu Kong, Bengt I. Lundqvist, and David C. Langreth, “Higher-accuracy van der waals density functional,” *Phys. Rev. B* **82**, 081101 (2010).
- ²⁰ Jiří Klimeš, David R Bowler, and Angelos Michaelides, “Chemical accuracy for the van der waals density functional,” *J. Phys. Condens. Matter* **22**, 022201 (2009).
- ²¹ Jia Chen, Andrew J. Millis, and Chris A. Marianetti, “Density functional plus dynamical mean-field theory of the spin-crossover molecule $Fe(phen)_2(NCS)_2$,” *Phys. Rev. B* **91**, 241111 (2015).
- ²² Arash A. Mostofi, Jonathan R. Yates, Giovanni Pizzi, Young-Su Lee, Ivo Souza, David Vanderbilt, and Nicola Marzari, “An updated version of WANNIER90: A tool for obtaining maximally-localised wannier functions,” *Comput. Phys. Commun.* **185**, 2309–2310 (2014).
- ²³ A. R. Wildes, H. M. Rønnow, B. Roessli, M. J. Harris, and K. W. Godfrey, “Static and dynamic critical properties of the quasi-two-dimensional antiferromagnet $MnPS_3$,” *Phys. Rev. B* **74**, 094422 (2006).
- ²⁴ A. R. Wildes, V. Simonet, E. Ressouche, G. J. McIntyre, M. Avdeev, E. Suard, S. A. J. Kimber, D. Lançon, G. Pepe, B. Moubaraki, and T. J. Hicks, “Magnetic structure of the quasi-two-dimensional antiferromagnet $NiPS_3$,” *Phys. Rev. B* **92**, 224408 (2015).
- ²⁵ Qiang Han, Turan Birol, and Kristjan Haule, “Phonon softening due to melting of the ferromagnetic order in elemental iron,” *Phys. Rev. Lett.* **120**, 187203 (2018).